

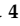




Article

Effect of Plasma Treatment on the Luminescent and Scintillation Properties of Thick ZnO Films Fabricated by Sputtering of a Hot Ceramic Target

Andrey P. Tarasov ^{1,*}, Abubakar M. Ismailov ², Makhach Kh. Gadzhiev ³, Ivan D. Venevtsev ⁴, Arsen E. Muslimov ¹, Ivan S. Volchkov ¹, Samira R. Aidamirova ², Alexandr S. Tyufyaev ³, Andrey V. Butashin ¹ and Vladimir M. Kanevsky ¹

¹ Shubnikov Institute of Crystallography, Federal Scientific Research Centre “Crystallography and Photonics”, Russian Academy of Sciences, 119333 Moscow, Russia
² Department of Physics, Dagestan State University, 367000 Makhachkala, Russia
³ Joint Institute for High Temperatures, Russian Academy of Sciences, 125412 Moscow, Russia
⁴ Department of Physics, Peter the Great St. Petersburg Polytechnic University, 195251 St. Petersburg, Russia
* Correspondence: tarasov.ap@phystech.edu

Abstract: The paper presents the results of a comprehensive study of the structural-phase composition, morphology, optical, luminescent, and scintillation characteristics of thick ZnO films fabricated by magnetron sputtering. By using a hot ceramic target, extremely rapid growth (~50 μm/h) of ZnO microfilms more than 100 μm thick was performed, which is an advantage for the industrial production of scintillation detectors. The effects of post-growth treatment of the fabricated films in low-temperature plasma were studied and a significant improvement in their crystalline and optical quality was shown. As a result, the films exhibit intense near-band-edge luminescence in the near-UV region with a decay time of <1 ns. Plasma treatment also allowed to significantly weaken the visible defect luminescence excited in the near-surface regions of the films. A study of the luminescence mechanisms in the synthesized films revealed that their near-band-edge emission at room temperature is formed by phonon replicas of free exciton recombination emission. Particularly, the first phonon replica plays the main role in the case of optical excitation, while upon X-ray excitation, the second phonon replica dominates. It was also shown that the green band peaking at ~510 nm (2.43 eV) is due to surface emission centers, while longer wavelength (>550 nm) green-yellow emission originates mainly from bulk parts of the films.

Keywords: ZnO; thick films; plasma treatment; scintillator; X-ray luminescence; photoluminescence; phonon replica; excitons; green luminescence; hot ceramic target



Citation: Tarasov, A.P.; Ismailov, A.M.; Gadzhiev, M.K.; Venevtsev, I.D.; Muslimov, A.E.; Volchkov, I.S.; Aidamirova, S.R.; Tyufyaev, A.S.; Butashin, A.V.; Kanevsky, V.M. Effect of Plasma Treatment on the Luminescent and Scintillation Properties of Thick ZnO Films Fabricated by Sputtering of a Hot Ceramic Target. *Photonics* **2023**, *10*, 1354. <https://doi.org/10.3390/photonics10121354>

Received: 21 September 2023

Revised: 30 November 2023

Accepted: 6 December 2023

Published: 8 December 2023



Copyright: © 2023 by the authors. Licensee MDPI, Basel, Switzerland. This article is an open access article distributed under the terms and conditions of the Creative Commons Attribution (CC BY) license (<https://creativecommons.org/licenses/by/4.0/>).

1. Introduction

Spectrometric detectors, together with the attached electronics, allow researchers to analyze amplitude spectra at all modern accelerators, as well as in astrophysical and neutrino experiments [1–5]. In particular, under conditions of extremely powerful energy flows—for example, in thermonuclear fusion installations—scintillation detectors are used as basic spectrometric detectors. Compared to semiconductor detectors, scintillation detectors have higher radiation resistance when exposed to ionizing radiation, greater ease of manufacturing, and a higher attenuation coefficient for γ - and X-ray radiation [5–9].

Currently, there is a need for scintillation materials with improved temporal and performance characteristics. In this sense, zinc oxide (ZnO) is a promising material due to its high radiation resistance, high transparency to its own radiation, and a record fast decay kinetics (less than 1 ns) for near-band-edge luminescence (NBEL) [9–14]. The radiation kinetics of traditionally used scintillators is not single-component—as a rule, along with a fast component, there is a slow component, which leads to false alarms of the detector

device. From this point of view, ZnO-based scintillators may be attractive as potentially capable of providing a high ratio of the intensities of fast and slow components.

Due to the ZnO polymorphism, in addition to bulk crystals, it is possible to produce a wide morphological range of nano- and microstructures with good optical and structural homogeneity such as arrays of 0D quantum dots, 1D rods (whiskers, wires, and the like), 2D plate-like crystals and microcrystals, nano/micro films, powders and ceramic samples, etc. [15–26]. At the same time, each type of morphology has its own advantages and disadvantages in terms of scintillation applications. In particular, intense NBEL under X-ray excitation is observed only in ZnO samples of high crystalline quality, such as bulk crystals [27,28], 1D and 2D nano- and microcrystals [28–31], or doped ZnO ceramics [32–34]. A disadvantage of bulk crystals in this sense is the presence of a slow component in the visible range of the luminescence spectrum, along with the fast NBEL component [27,35]. In addition, the technological difficulty of manufacturing bulk ZnO crystals is known [23,36–38], which limits their use. Arrays of 1D and 2D ZnO nano/microcrystals, demonstrating a predominantly fast excitonic emission, have low transmission in the near-band-edge region, which is due to increased light scattering in a highly inhomogeneous structure, resulting in its stronger reabsorption [30]. From this point of view, ZnO film structures, with their increased transparency for NBEL, have an advantage over arrays of nano/microcrystals. The ability to reproducibly produce ZnO films of different thicknesses within a few micrometers contributes to the achievement of high spatial resolution and minimal sensitivity to background emission when detecting certain types of ionizing radiation, e.g., α -particles [39].

Among the problems of using ZnO films for detecting ionizing radiation, one can note their poor emission characteristics compared, for example, with arrays of ZnO nano/microcrystals or doped ceramics [40]. A common disadvantage of ZnO films is the much stronger visible luminescence component as compared to the NBEL band—this is especially pronounced in relatively thick micron-scale films [41,42]. However, the major drawback is, in general, the low light output when irradiated with γ - and X-rays. To reliably detect such radiation in practical applications, a sufficiently large volume of scintillation material is required—a continuous ZnO layer at least 20 μm thick. At the same time, obtaining such “thick” films requires maintained stable synthesis parameters over a long deposition time and is complicated by the cracking of the films and their peeling off from the substrate. In [43], a method was first proposed for the synthesis of ZnO films using a hot target. This method provides an extremely high growth rate of the films due to cluster emission and good adhesion to a sapphire substrate. However, due to the tendency of the deposit to amorphize, as well as nonstoichiometry, such films demonstrated either a complete absence of luminescence or a broad band of visible luminescence resulting from lattice defects [41,42]. Such emission has slow decay kinetics and is not of interest for scintillation applications. Post-growth annealing at temperatures of 400–1000 $^{\circ}\text{C}$ resulted in an improvement in the crystalline quality of the films and an increase in their transmission level, but did not allow an increase in the ratio of the fast UV and slow visible luminescence components. Taking into account significant mechanical stresses and a high concentration of point defects in ZnO films obtained at high growth rates, it seems to us advisable to use short-term annealing at ultra-high temperatures, since this will significantly promote stress relaxation.

In the present work, we used low-temperature plasma treatment of ZnO films as that kind of post-growth processing. In particular, we studied the effect of plasma treatment on the structural, morphological, optical, luminescent, and scintillation properties of thick (more than 100 μm in thickness) ZnO microfilms grown on sapphire substrates by the sputtering of a hot ceramic target. It was shown that such a treatment has a positive effect on the crystalline quality and luminescent properties of the fabricated films. In particular, the films revealed an intense NBEL band with fast decay kinetics under both optical and X-ray excitations, while possessing a good degree of transparency. The spectral features of the films’ emission obtained under both excitation types were compared and an

interpretation of the luminescence mechanisms was given. It was shown that the main role in NBEL is played by phonon replicas of free exciton radiation. Some conclusions about visible luminescence of the films were also given.

2. Materials and Methods

Growth of ZnO films on $R(10\bar{1}2)$ -plane sapphire substrates was carried out by the technique of a magnetron sputtering of a hot ceramic target [43]. For this, the VATT AMK-MI automated magnetron complex (FerriWatt, Russia) was used with the following process parameters: substrate temperature, 830 °C; pressure, 1 Pa; gas flow rate, ~8 l/h; discharge current, 500 mA; deposition time, 2 h. The target was a sintered ZnO ceramic disk (of 99.999% purity). The power density on the target was 53.5 W/cm². The substrates were heated by a resistive heater (nichrome); the temperature was controlled using a chromelalumel thermocouple. Next, the ZnO samples were cut into several parts and for testing different methods of post-growth treatment. In this work, samples were processed in low-temperature high-enthalpy argon plasma. A low-temperature plasma generator with a self-adjusting arc length and an expanding channel of the output electrode was used as a plasma source [44]. The total electric power of the arc discharge was 10 kW and the plasma-forming gas consumption rate was 3 g/s. The parameters of the plasma flow were determined by spectral methods using the AvaSpec 2048 three-channel fiber-optic spectrometer. The spectrometer was used to monitor radiation (with a periodicity of 3–4 spectra per second) along the plasma flow axis in a wavelength range of 240–1000 nm with a spectral resolution of 0.2–0.5 nm. The presence of a large number of ArI atomic argon lines in the spectra of argon plasma allowed us to measure temperature by the Boltzmann exponent method [45]. The electron concentration in the axial region of the plasma jet can be estimated from the half width of the H_α and H_β lines. A mass-average temperature of the plasma flow in the interaction zone was ~7 kK at an electron concentration of 10¹⁵ cm⁻³.

Polishing of the sample was carried out using a chemical-mechanical method [46]. The study of surface morphology was carried out on a Jeol Neoscope 2 scanning electron microscope (SEM) equipped with an energy-dispersive X-ray (EDX) microanalyzer. Structural studies of the films were performed using the X-ray diffraction (XRD) method. XRD patterns were obtained using a PANalytical X'Pert Pro MRD diffractometer in the Bragg–Brentano geometry. Radiation from a copper anode (CuK_{α2}, λ = 1.54 Å) was used (voltage, 40 kV; current, 40 mA). The measuring angle range (2θ) is 30–80°. During the XRD measurements, the samples were rotated around their axis at a rate of 2 rps. XRD patterns were analyzed by means of the High Score Plus program, using the ICDD database (PDF 01-079-0205).

Spectra of X-ray excited luminescence (XRL) were measured using reflection geometry under continuous-wave (*cw*) X-ray excitation. The X-ray tube had a tungsten anode and a beryllium window; tube voltage and current were 40 kV and 10 mA, respectively (under these parameters, most of the radiation is bremsstrahlung). Registration tract contained an MDR-2 optical monochromator and Hamamatsu H8259-01 photon counting head. The emission spectrum was recorded in the range of 350–650 nm. Total transmittance spectra were recorded in a range from 350 to 1100 nm using SPECORD 200 PLUS double beam spectrophotometer equipped with an integrating sphere. XRL kinetics were measured under pulsed X-ray excitation using the time-correlated single photon counting method. The setup used was a slightly modified version of the one described in [47]. The excitation pulse had a width of around 800 ps. Emission was registered in integral mode (monochromator was not used) by Hamamatsu R3235-01 photomultiplier tube.

Photoluminescence (PL) of the samples was studied at low and high excitation intensities. To obtain PL spectra at low *cw* excitation intensity, we used light with a wavelength of 315 nm, spectrally selected in a Varian Cary Eclipse spectrofluorometer equipped with a xenon lamp and a photomultiplier detector. Relatively high excitation intensities were provided by a third harmonic (355 nm) of a pulsed Nd:YAG laser (pulse duration, 10 ns; pulse repetition rate, 15 Hz). The power densities created on the sample's surface in this

case were in the range of 5–110 kW/cm². The emission of the sample was collimated to the entrance slit of a monochromator coupled to a Peltier-cooled charge-coupled device camera. More details about our PL and XRL measurements can be found elsewhere [30,31].

3. Results

Figure 1 shows the SEM images of one of the grown ZnO films. According to the SEM data, the grown film has a thickness more than 100 μm and a columnar structure with micropores up to 10 μm in size and up to 50 μm in depth (Figure 1a,b). Elements of the columnar structure are formed by flat *c*-oriented ZnO crystallites layered on top of each other. The specific morphology of the film can be explained by the peculiarities of the synthesis process. During magnetron sputtering with the use of a hot target, radiation-accelerated processes of diffusion and evaporation are added to the emission of atoms and clusters from the target surface as a result of bombardment [43]. In this case, the target is heated to a temperature above 1000 °C and under these conditions can emit not only individual particles, but also their clusters. The presence of clusters radically changes the growth conditions of the films. The mobility of massive clusters is achieved due to the high temperature of the substrate and the electrostatic interaction of the clusters [48]. In this case, the high intensity of the incident flux of individual particles and their clusters leads to prevailing growth of the ZnO deposit along the shortest distance between the source and the substrate [49]. This causes the deviation of the axis of the morphological texture of the film from the normal to the substrate (Figure 1a).

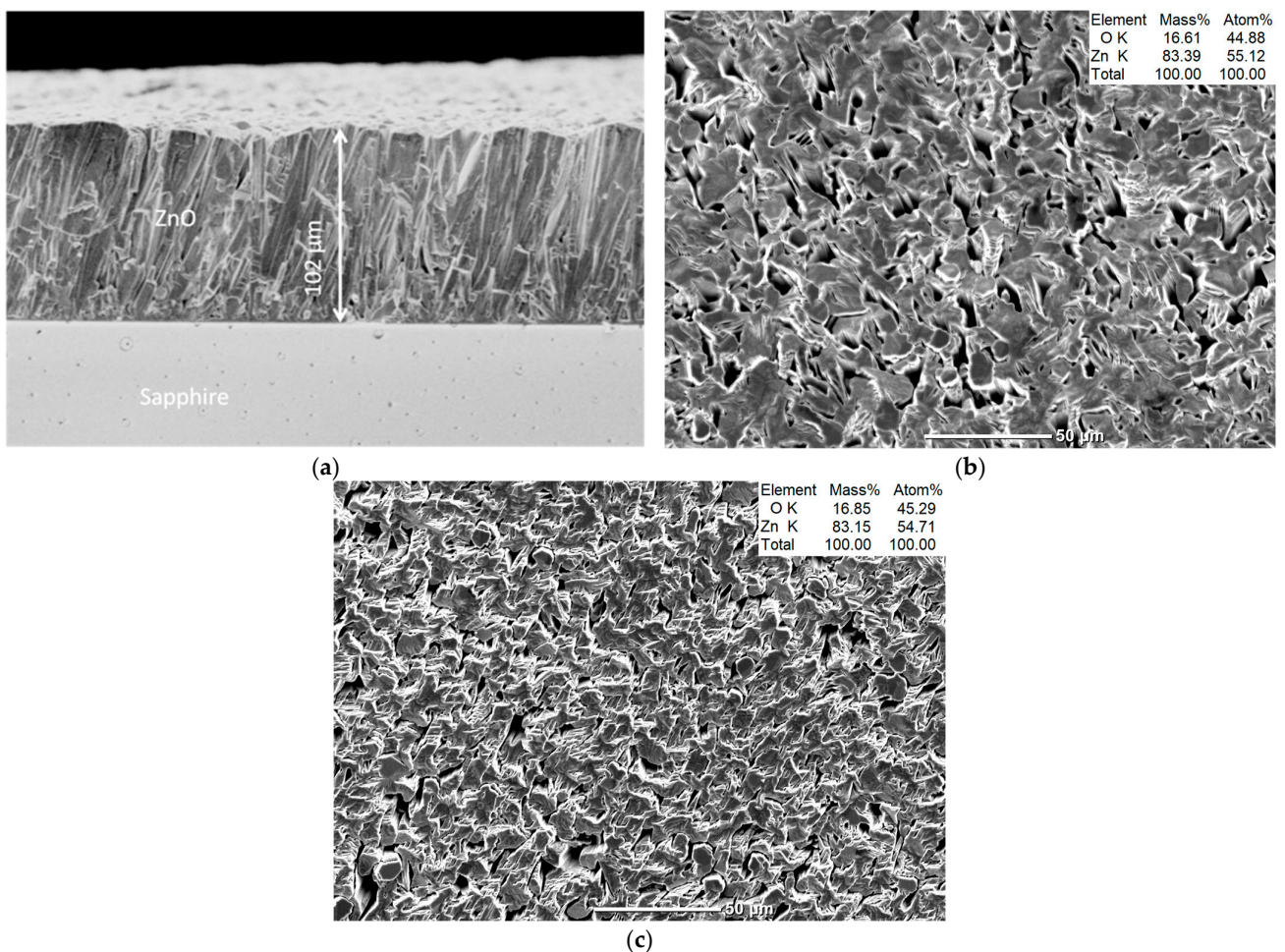


Figure 1. SEM images of a thick ZnO film: (a) A cross section of the as-grown film; (b) surface of the as-grown film; (c) surface of the plasma-treated film. Figure (b,c) are supplemented with the EDX data (in the insets).

During plasma treatment, the surface morphology of the film became more developed (Figure 1c). The change in surface morphology had the character of etching—the appearance of steps is observed on the side surfaces of the columns. At the same time, EDX microanalysis revealed the preservation of the relative zinc and oxygen contents after plasma treatment (see the insets in Figure 1b,c), which indicates congruent evaporation of the material.

According to the XRD data (Figure 2), a highly textured *c*-oriented ZnO film is formed as a result of the deposition process. After plasma treatment of the films, the prevailing (002) orientation was retained. The appearance of an additional intense reflection from (110) plane, as well as reflections of the sapphire substrate, is associated with the exposure of the peripheral part of the film to the illumination spot. The epitaxial (110) orientation of ZnO grown on the *R*-plane sapphire presumably takes place in thin peripheral layers [50].

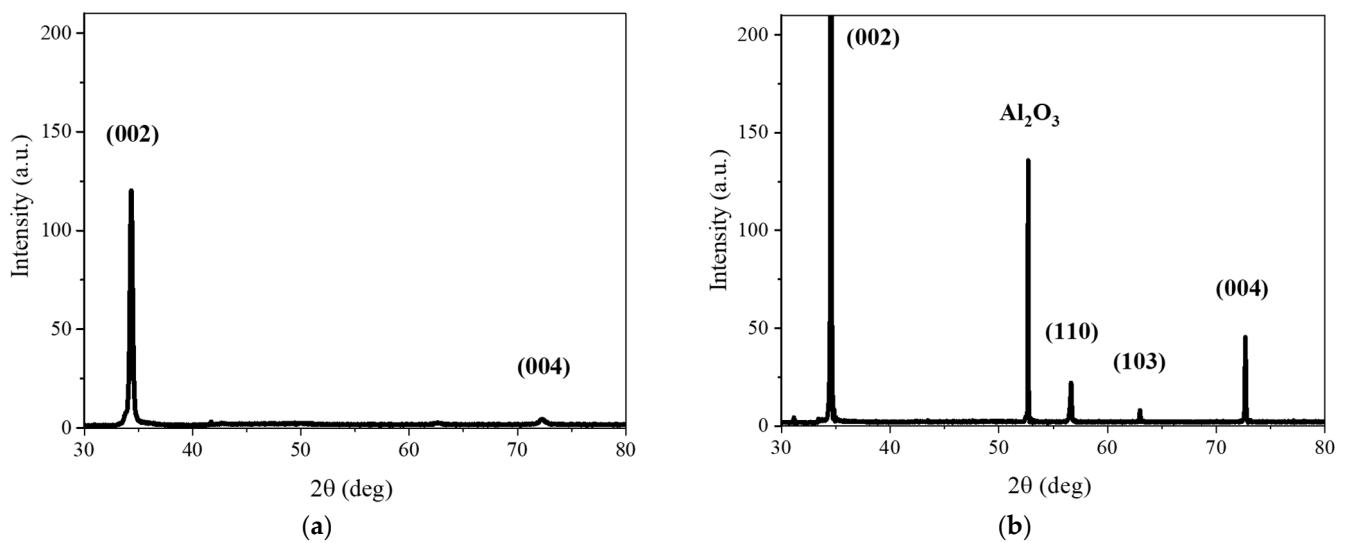


Figure 2. XRD patterns of the as-grown (a) and plasma-treated (b) ZnO films grown on *R*-plane sapphire.

The sizes of coherent scattering regions (CSRs) in the samples under study were estimated using the Scherrer formula [51–53]:

$$D = \frac{k \cdot \lambda}{\beta \cdot \cos \theta} \tag{1}$$

where *D* is the average size of CSRs, which can be less than or equal to the grain size; *k* is the dimensionless particle shape coefficient (Scherrer constant); λ is the wavelength of copper X-ray radiation; β is the width of the reflection at half maximum; and θ is the diffraction angle.

Evaluation using (1) showed that the average size of the CSRs increases after plasma treatment. In particular, for the as-grown and plasma-treated films, $D \approx 31.9$ and 133.6 nm, respectively, in the $\langle 002 \rangle$ direction. A trend toward increasing CSR size is also observed in the case of the $\langle 103 \rangle$ direction: $D \approx 123.1$ nm. The appearance of the (110) reflection also indicates a more intense growth of the lateral surface of the columns. These results indicate a significant increase in the degree of crystalline perfection of samples subjected to plasma treatment—this can be easily seen from the shape of the XRD peaks, which become significantly narrower after treatment. Estimation of microstresses in the films, using the Stokes–Wilson formula ($\beta = 4\epsilon \cdot \tan \theta$, where ϵ stands for the maximum value of a microstress), taking into account the contribution made by scattering at crystallite boundaries, suggests a decrease in mechanical stresses in the films after plasma treatment. In particular, the value of microstresses for the as-grown film is 1.7–1.9 times higher than that for the plasma-treated film. Herewith, the most dramatic changes obviously affected

the near-surface regions of the film that directly interact with the plasma. Taking into account the high temperature of the plasma (more than 5000 K) and the relatively non-destructive changes in the structural and morphological properties of the films (etching, recrystallization, and lack of melting), the existence of an effective heat sink between the sample and the holders can be assumed—therefore, only the upper part of the film, up to a thickness of ~15–20 μm , was effectively heated.

Figure 3 shows the PL spectra in the near UV and visible regions of the film before and after the plasma treatment, which were registered under low-intensity *cw* excitation using a Xe lamp (Figure 3a) and a relatively high-intensity pulsed laser excitation (Figure 3b,c). Under low-intensity excitation, luminescence of the samples consists of a narrow UV emission band, which is near-band-edge luminescence (NBEL) of ZnO [54,55], and a wide green emission band spanning from ~450 to 650 nm, which is usually attributed to intrinsic defects of ZnO crystal lattice and called defect or deep-level luminescence (DL) [54–56]. When comparing these spectra, the first thing that catches the eye is the significant difference in the intensity of the emission bands. Namely, plasma treatment resulted in a significant weakening of the DL component (by 16 times in the band's maximum), with an increase in the intensity of NBEL band (by 1.5 times). Moreover, while the NBEL component peaked at ~379 nm (3.27 eV) for both cases, the DL component redshifted from ~510 nm (2.43 eV) to 525 nm (2.36 eV) as a result of a plasma treatment.

Upon pulsed laser excitation, DL was practically absent even in the case of the as-grown film—only a weak broad band peaking at 510 nm was observed (see the inset in Figure 3b). Such a cardinal change in the film's emission profile between two optical excitation cases can be explained by two effects: (i) saturation of DL centers at the high-density excitation and (ii) a decrease in the thickness of the depletion layer as a result of the energy band flattening. In the second case, electron–hole pairs, intensively created by photons with energy greater than the band gap, neutralize the excess charge on the semiconductor surface—the existence of this charge, in the absence of illumination, causes bending of the energy bands and formation of the depletion layer. The straightening of the energy bands is accompanied by a partial deactivation of DL centers located near the surface and an increase in the probability of interband transitions. All this results in a relative increase in the UV component as compared to the visible one.

In view of this, the visible part of the film luminescence spectra before and after plasma treatment is practically the same, and one can focus on the study of NBEL (main part of Figure 3b). Under this type of excitation, the NBEL band peaks at 381 nm. Moreover, in addition to the main maximum, a long-wavelength shoulder is noticeable in the region of 390–400 nm. Similar to the case of low-intensity excitation, NBEL has intensified after plasma treatment when being excited by a laser, and the band intensity increased by more than 2 times (in the maximum).

Figure 3c shows the evolution of NBEL of the plasma-treated film with increasing power density ρ_{exc} of pulsed laser excitation. As ρ_{exc} increases, the long-wavelength shoulder of the NBEL band becomes more and more distinct and even forms a separate band with a clear maximum. In this case, the peak intensity of the long-wave band grows faster in comparison with the main short-wavelength component. Nevertheless, the integrated intensity of the entire NBEL shows a linear increase up to ~80 kW/cm^2 , after which it begins to saturate.

To use a ZnO film as a scintillator, it is first necessary to achieve high intensity of the fast NBEL component under X-ray excitation and high transmittance, which is important when using a scintillator in transmission geometry. As was mentioned in the Introduction, thick ZnO films that were not exposed to plasma treatment do not show NBEL and, hence, are not of interest for us (see, e.g., [41,42] for such a study). In order to smooth the surface and increase transmission of the films, the plasma-treated samples were processed by a chemical-mechanical method. During the etching process, the film thickness decreased to 80 μm , but the porosity was preserved. The roughness of the smooth areas of the film decreased to values of the order of 5 nm.

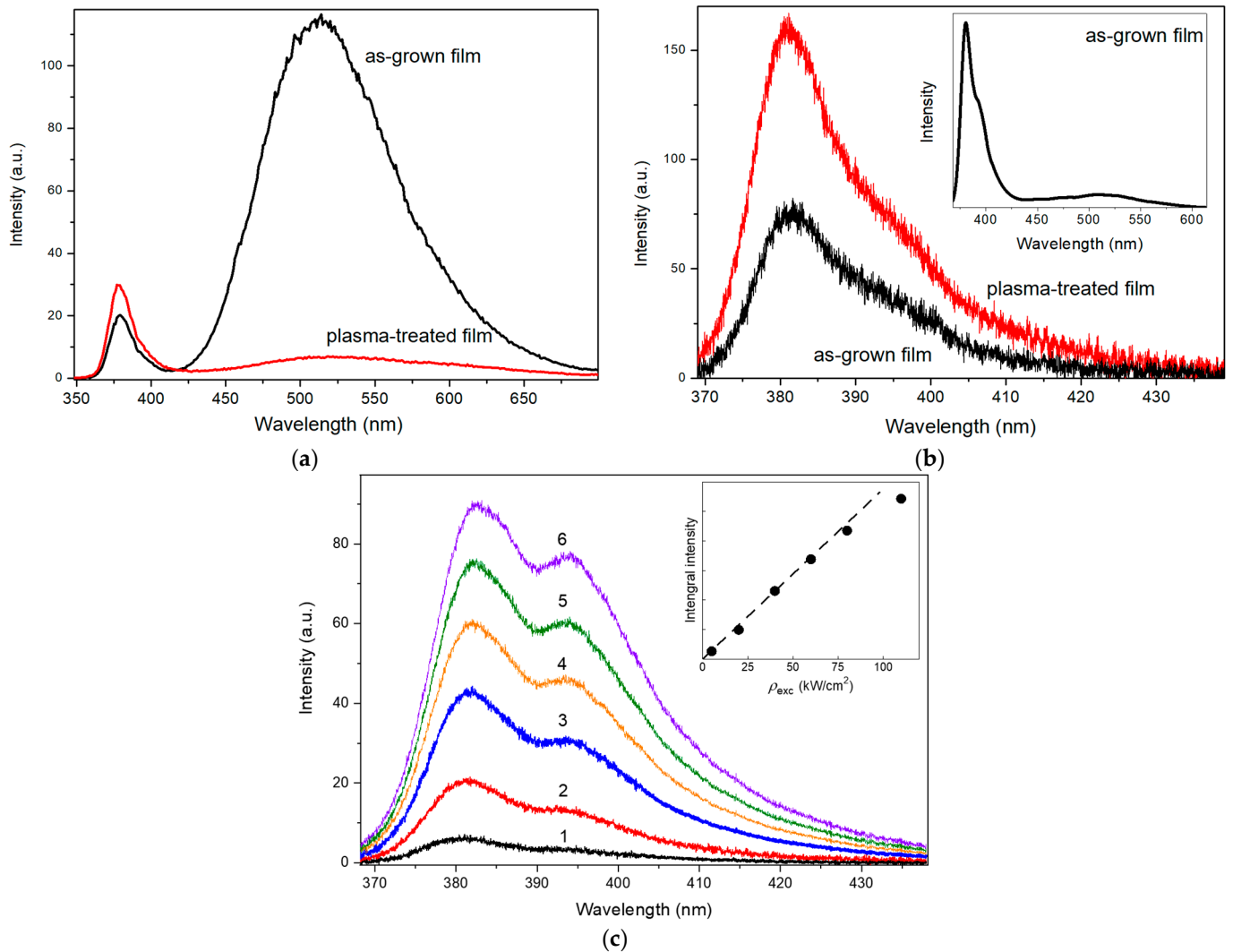


Figure 3. Room-temperature PL spectra of the ZnO film: before (black) and after (red) plasma treatment at low-intensity *cw* excitation (a) and relatively high-intensity pulsed laser excitation at $\rho_{exc} \approx 30 \text{ kW/cm}^2$ (b); after plasma treatment at different excitation power densities ρ_{exc} : ~ 5 (1), 20 (2), 40 (3), 60 (4), 80 (5), 110 (6) kW/cm^2 (c). The inset in (b) shows the PL spectrum of the initial film in UV and visible ranges. The inset in (c) shows the dependence of the NBEL integral intensity of the plasma-treated film on ρ_{exc} .

XRL spectra of the plasma-treated sample before and after polishing are shown in Figure 4a (curves 1 and 2, respectively). In this case, ZnO film’s emission spectra also contain NBEL and DL bands. However, both bands are redshifted as compared to PL. The NBEL component peaks at 389 nm and 392 nm before and after polishing, respectively. The DL component has a maximum at $\sim 550\text{--}570 \text{ nm}$ and exhibits green-yellow tint. The NBEL band’s intensity of the film after polishing is around half of that in the case before polishing. The DL band has nearly the same intensity in both cases. The long-wavelength shoulder of the DL band is due to the contribution of substrate emission in the red region. The XRL spectra of a sapphire substrate is presented in Figure 4a (curve 3) as well.

Figure 4b shows XRL decay kinetics of the film before (curve 1) and after (curve 2) polishing. Both curves have a similar structure; they consist of a fast component with a decay time of 0.8–0.9 ns and a slow component with a decay time of the order of 1 μs , which has slightly higher relative intensity in the case of a polished film.

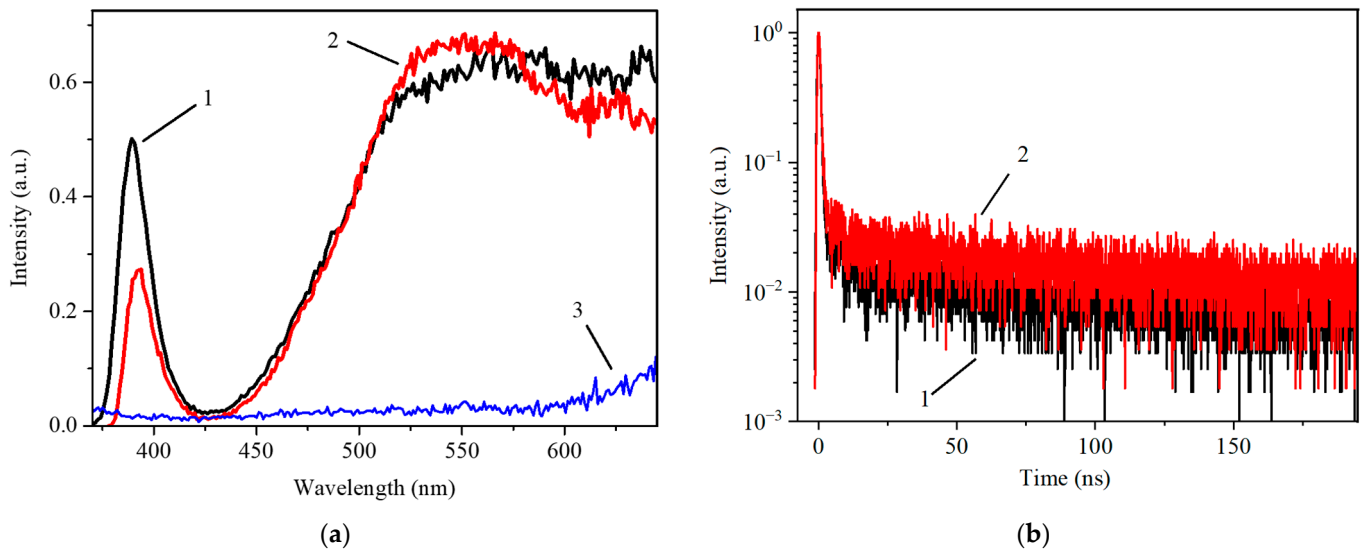


Figure 4. XRL spectra (a) and decay kinetics (b) of the plasma-treated ZnO film before (curve 1) and after (curve 2) polishing and of a sapphire substrate (curve 3).

Figure 5 shows the total transmittance spectra for the plasma-treated film before and after polishing (curves 1 and 2, respectively). In both cases, the absorption edge is nearly the same and equals ~387 nm. Polishing resulted in an increase in film transmittance. Despite the apparent similarity in the shape of the spectra, the increase in transmittance was different depending on the spectral interval. The inset in Figure 5 plots the transmittance ratio in the range of 390–720 nm for the film after and before polishing. One can see that the transmittance in the near UV range increased after polishing by more than 2 times. In the visible range, the increase in transmittance was ~20%.

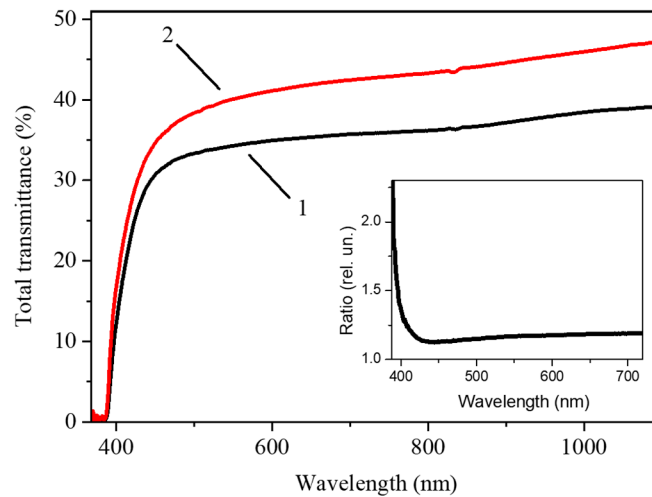


Figure 5. Total transmittance spectra of the plasma-treated ZnO film before (1) and after (2) polishing. The inset shows the ratio of (2) to (1).

In order to interpret the luminescence mechanisms of the fabricated films, their emission spectral features were compared in different excitation regimes. Figure 6 compares the NBEL spectra of the plasma-treated film registered under X-ray and optical (low- and high-intensity) excitation types. Spectra are normalized to maximum. Despite the small difference in the wavelengths of the bands (~2 nm) for both cases of optical excitation, the similar shape of the NBEL bands attracts attention, which indicates an identical spectral composition and the admissibility of using pulsed laser excitation with relatively low power densities in the analysis of films’ luminescence mechanisms. In the XRL spectrum,

both the position and shape of the NBEL band appear to be different from the case of optical excitation. The band has a more symmetrical shape and is longer wavelength by 10 nm (84 meV) and 8 nm (67 meV), respectively, compared to low- and high-intensity photoexcitation, which is comparable to the energy of the LO phonon in ZnO (72 meV). The band's wavelength under X-ray excitation corresponds to the spectral region of the long-wavelength shoulder of NBEL in the PL spectra.

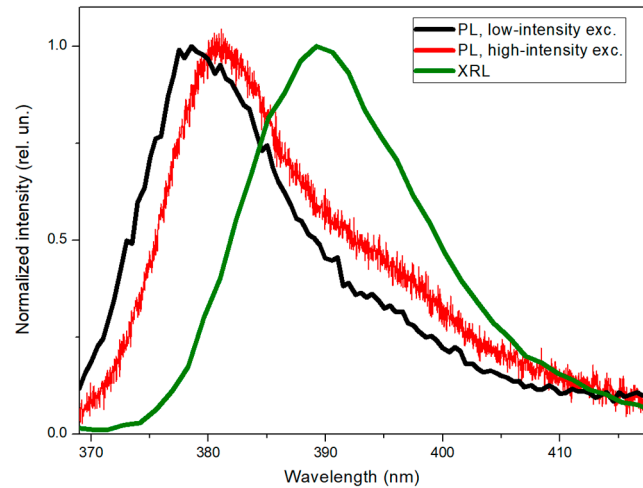


Figure 6. NBEL spectra of the plasma-treated ZnO film, recorded at low-intensity *cw* excitation (black), relatively high-intensity pulsed excitation with $\rho_{exc} \approx 30 \text{ kW/cm}^2$ (red), and X-ray excitation (green).

Figure 7a shows NBEL spectra of the as-grown film at different temperatures (the most representative spectra are shown) registered under laser excitation with $\rho_{exc} \approx 25 \text{ kW/cm}^2$ (the case of the plasma-treated film was similar). The NBEL pattern at $T \sim 80 \text{ K}$ is typical for nominally undoped ZnO microcrystals at this temperature [57–59]. In particular, three emission bands are clearly distinguishable (indicated as A_i in Figure 7, where $i = 1, 2, 3$) with the energies of 3.356, 3.311, and 3.234 eV (the corresponding wavelengths are 369.4, 374.5, 383.4 nm). Moreover, there is a clear short-wavelength shoulder of the A_1 band at $\sim 3.37\text{--}3.38 \text{ eV}$ (367–368 nm). These bands are due, respectively, to the recombination of bound excitons (A_1), the first phonon replica of free exciton radiation ($X\text{-LO}$) with a possible contribution of emission involving surface states (A_2), and the second ($X\text{-2LO}$) phonon replica of free exciton radiation (A_3). The feature at the low-energy tail of the A_1 band can be ascribed to free exciton emission. Taking into account low surface-to-volume ratio of the films, the contribution of phonon replicas of emission bands related to surface defects in the energy range above $\sim 3.25 \text{ eV}$ is probably small.

In Figure 7b, the temperature behavior of the emission energy of the marked bands is plotted. All these bands can be traced separately up to $T \sim 180 \text{ K}$. After this, the maximum of the A_2 band ceases to be clearly distinguishable, and at $T \sim 230 \text{ K}$ the A_1 and A_2 bands merge into one wide band (the maximum of the combined band is shown by empty circles in Figure 7b). The A_3 band can be traced up to $T \sim 250 \text{ K}$.

In order to establish the nature of the short-wavelength (main) NBEL band at room temperature (RT), the temperature dependences of the band gap energy $E_g(T)$ or exciton transition energy $E_X(T)$ for the sample can be useful. In this work, we deal with ZnO microstructures fabricated under normal conditions without the use of additional doping. In addition, the films' NBEL pattern is typical for microcrystalline ZnO at low temperatures and low excitation intensities. In this case, we can use the data on $E_g(T)$ or $E_X(T)$ for bulk or microcrystalline ZnO to interpret the luminescence mechanisms of the studied samples at various temperatures, including RT [59]. In particular, $E_X(T)$ obtained for a bulk ZnO crystal in [57], valid for microcrystalline ZnO [59], is shown in Figure 7b as a solid line. In Figure 7b, the temperature behavior for the energies of the $X\text{-LO}$ and $X\text{-2LO}$ bands is also plotted, according to the expression [58]

$$E_{X-mLO}(T) = E_X(T) - mE_{LO} + \left(\frac{5}{2} - m\right)k_B T, \quad (2)$$

where $m = 1$ and 2 for X-LO and X-2LO processes, respectively, E_{LO} is the energy of the LO phonon (72 meV in ZnO), and $E_X(T)$ is taken from [57].

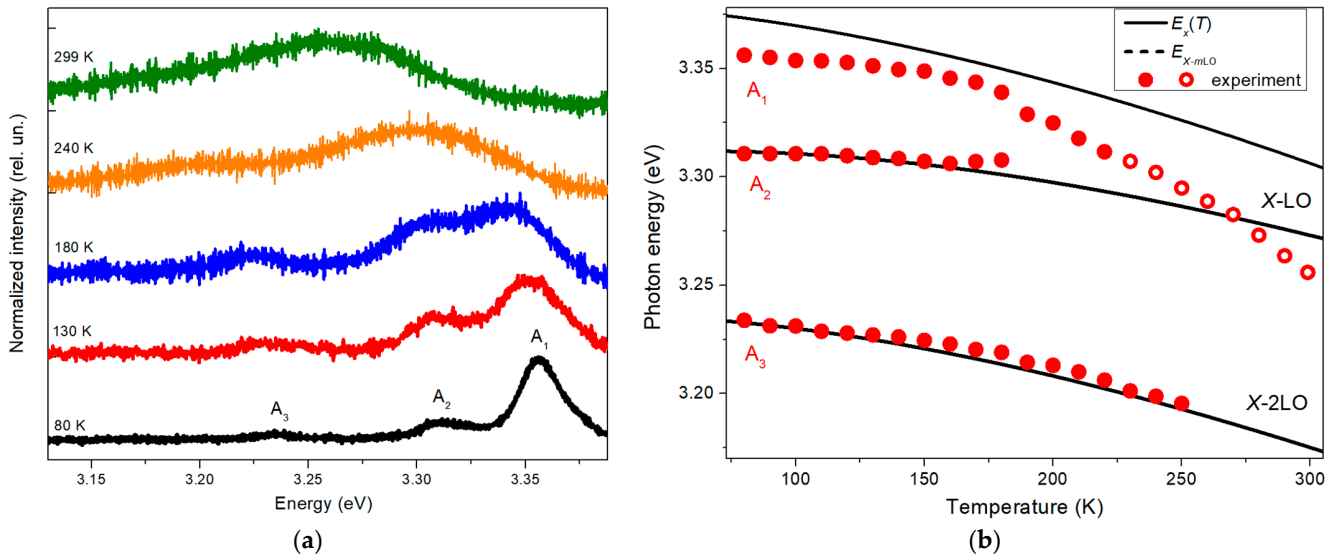


Figure 7. (a) NBEL spectra of the as-grown film at different temperatures under pulsed laser excitation at $\rho_{exc} \approx 25 \text{ kW/cm}^2$; (b) photon energy vs. temperature for the emission bands A_1 , A_2 , and A_3 in (a) (circles); open circles indicate a combined $A_1 + A_2$ band. Dashed lines indicate theoretical energies $E_{X-LO}(T)$ and $E_{X-2LO}(T)$ using $E_X(T)$ from [57] (indicated with a solid line).

It can be seen that the plotted curves (Figure 7b) describe the observed emission bands well. Firstly, the temperature behavior of A_3 band confirms an attribution of it to the X-2LO process. Secondly, the A_2 band quite strictly follows the energy $E_{X-LO}(T)$, which proves the main contribution of the first phonon replica X-LO to this band. Finally, the behavior of the A_1 band, which was attributed to the BX radiation at $\sim 80 \text{ K}$, is rather indicative. At the initial temperature rise from 80 to 170 K, the A_1 band approaches $E_X(T)$ from 17 meV to 9 meV. At $T > 160 \text{ K}$, the band rapidly moves away from $E_X(T)$. Such behavior can be explained by thermally dissociation of BXs as the temperature rises. Above $T \sim 170 \text{ K}$, when most of the BXs dissociated, the A_1 band is mainly due to zero-phonon exciton recombination; its energy approaches the A_2 band’s spectral region due to overlapping of the bands. At $T > 250 \text{ K}$, the A_3 band merges into the combined $A_1 + A_2$ band, which possibly causes the redshift of the combined band’s maximum away from theoretical dependence $E_{X-LO}(T)$. Thus, emission of the fabricated films at RT under optical excitation is predominantly due to phonon replicas of free exciton emission (mainly X-LO), which corresponds to the case of bulk ZnO [54].

4. Discussion

As was indicated in the Introduction, previously studied thick ZnO films obtained by the same method and not subjected to plasma treatment exhibited a very weak NBEL or its complete absence under X-ray excitation [41,42]. High-temperature annealing, although it improved the crystalline quality of the films, led to intensification of DL due to different rates of desorption of zinc and oxygen elements and did not allow the appearance of any significant NBEL signal [41,42]. In this regard, the use of plasma treatment has proven useful for improving the optical quality of thick ZnO films and may be an important step towards the development of ZnO-based thick film scintillators. Such processing resulted in the appearance of the intense NBEL with a subnanosecond decay time under X-ray excitation. The NBEL intensity of the fabricated films is within an order of magnitude

comparable to that for ZnO:Ga ceramics [30], although the ceramic samples are significantly thicker than the films studied. In addition, the transmission of the films is noticeably higher than that in the case of ZnO micro- and nanostructures [30] and comparable, although still lower, with the transmission of ceramics.

Plasma treatment allowed us to increase the NBEL intensity and significantly weaken the DL band under optical excitation, due to improvement of the optical quality of the films in the near-surface regions. The impact of a plasma jet can mainly be reduced to the influence of two factors: high temperature and jet pressure. High temperature promotes intense sublimation of the material from the surface of the sample, bypassing the melting stage. In this case, it would be logical to assume incongruent evaporation of the material, which should be reflected in an increase in the concentration of point defects and a rise in the DL band intensity. However, the opposite effect is observed; the weakening of DL in combination with the EDX microanalysis data, indicating only minor changes in the composition of the surface layers after plasma treatment, suggest congruent evaporation. Calculations given in [60] show that under the post-growth processing conditions used in the work, the pressure of the plasma jet flow on the sample can reach 15 kPa. This may be a key factor promoting congruent evaporation. The most defective near-surface regions of the films are etched first, due to the low energy of desorption of the components in them. As a consequence, firstly, this results in a decrease in the concentration of near-surface defects that can participate in DL and/or in nonradiative exciton recombination. Secondly, it reduces the thickness of the depletion layer associated with these defects, where the formation of excitons is difficult due to the spatial separation of electrons and holes. In addition, a decrease in the grain boundary surface due to the growth of crystallites reduces the volume of the structure occupied by depletion regions.

PL studies allowed us to understand the structure and nature of NBEL of the fabricated films at RT both under optical and X-ray excitations. Temperature measurements carried out under pulsed laser excitation revealed that NBEL is formed mainly by X-LO and X-2LO emission processes. In particular, X-2LO radiation appears as a long-wave shoulder to the main band formed by X-LO radiation, while X-LO radiation forms the main part of UV luminescence of the films studied under this type of excitation. The linear growth of the integral intensity of the NBEL band vs. the excitation power density ρ_{exc} , despite the different rates of growth for the main (short-wavelength) band and its long-wavelength shoulder (long-wavelength band), confirms the participation of the same particles (excitons, in this case) in both channels of radiation. Herewith, a redistribution of excitons occurs between these channels; with the increasing excitation intensity, more and more excitons participate in the X-2LO process. Note that the relatively low intensities of pulsed laser excitation used in the experiment and the large thickness of the films make it possible to avoid the formation of electron-hole plasma and expect the participation of excitonic mechanisms in luminescence. An assessment of the density of electron-hole pairs created by photoexcitation taking into account their possible diffusion (see, e.g., [31,61]) gives values, in the order of magnitude not exceeding 10^{18} cm^{-3} , i.e., the threshold Mott density for ZnO [62].

Judging by the identity of the shape of the PL spectra registered under low- and high-intensity photoexcitation, the nature of NBEL in these two cases is apparently similar. The small difference between the NBEL band positions in these cases is most likely due to the relative increase in the X-2LO emission intensity with an increasing excitation level, as confirmed by a more noticeable long-wavelength shoulder of the main maximum and by the measurements at different ρ_{exc} . A slight narrowing of the ZnO band gap as a result of film heating by laser radiation cannot be ruled out either.

It was previously estimated that the density of electron-hole pairs created under low-intensity optical and X-ray types of excitation in our experiment is approximately the same and amounts to 10^{13} – 10^{14} cm^{-3} [31]. Thus, a comparative analysis of all three cases of excitation is permissible for the thick ZnO films under study and, most likely, in general, in the case of fairly massive ZnO microstructures.

Under single-photon excitation due to the strong absorption of UV light (the absorption coefficient of UV photons in ZnO is $\sim(1-2)\cdot 10^5 \text{ cm}^{-1}$ [54]), the PL of the films, in contrast to XRL, is excited in a narrow near-surface layer. Meanwhile, X-ray radiation has a fairly large penetration depth; X-ray quanta can penetrate the films right down to the substrate (see Figure 4a and related comments in the text). This distinguishes microfilms from the case of ZnO structures with nanosized or submicron crystallites, where the portion of material volume participating in both PL and XRL can be rather high, and, hence, the PL and XRL spectra can be similar [30,31]. Thus, the strong difference in the position of the NBEL band in the case of XRL and PL of the films (see Figure 6) is apparently associated with the dominant contribution of radiation excited in the bulk of the films to their XRL. Such radiation travels a considerable distance in the film before leaving it, which results in its strong absorption. In this case, light with wavelengths closer to the fundamental absorption edge of the material is absorbed more intensely (the absorption edge, judging by the UV-vis spectroscopy results, is located at $\sim 387 \text{ nm}$). This leads to a relative decrease in the intensity of the short-wavelength edge of the NBEL band and, as a consequence, to a redshift of its maximum to the region of $\sim 390 \text{ nm}$. As a result, the main portion of NBEL under X-ray excitation is formed by X-2LO radiation.

The polishing of the films affected the degree of their transmittance and emission parameters and made it possible to draw conclusions about some additional aspects of the optical properties of the films and their modification as a result of plasma treatment. In particular, after polishing, the transmittance in the visible part of the spectrum increased by 15–20%, which correlates with the proportion of material removed as a result of polishing. In the near-band-edge region, polishing resulted in a much greater increase in transmission—more than 2 times. At the same time, after polishing, the NBEL intensity under X-ray excitation decreased by almost 2 times, while the DL band intensity remained virtually unchanged. All this speaks of a nonuniform distribution of UV emission centers throughout the film thickness. Namely, as a result of plasma treatment, they were formed mainly closer to the surface regions of the film. At the same time, the centers of visible emission excited by the X-ray source are apparently distributed more or less uniformly throughout the depth of the film.

The nonuniform distribution of NBEL centers may also be the reason of the redshift (by 2–3 nm) of the NBEL band after polishing. A more uniform distribution of NBEL centers along the depth of the polished sample leads to the fact that a significant portion of the UV radiation is formed in the bulk of the film. Such radiation experiences intense reabsorption, which leads to a redshift of the NBEL band in the XRL spectrum of the polished film as compared to the unpolished film, where UV light under X-ray excitation mainly originates from the near-surface regions.

From the point of view of the potential application of thick ZnO films as scintillation material, additional polishing, however, is not required. Such treatment results in a significant drop in the NBEL intensity while retaining the DL intensity rather high.

The obtained PL and XRL data also allow one to come to some conclusions about the localization of radiative defect states responsible for individual emission components in DL of the fabricated films. After plasma treatment, the DL band under low-intensity optical excitation redshifted towards longer wavelengths by $\sim 15 \text{ nm}$ (Figure 3a), i.e., towards the DL maximum observed under X-ray excitation. At the same time, due to the deep penetration of X-ray quanta, XRL reflects to a greater extent the bulk radiative states of the sample; the surface of the sample has less influence on the XRL character. At the same time, plasma treatment has a greater effect on the film surface and its near-surface regions, eliminating the corresponding defect emissive states and enhancing interband transitions in this region (see Figure 3a). Thus, we can suggest that the bright DL component peaking at 510 nm, observed in the PL spectra of the samples untreated in plasma, is provided by surface defect states, while the source of longer wavelength radiation is largely the bulk states of the films. This conclusion correlates with XRL data obtained for ZnO whiskers,

which have a large surface-to-volume ratio and, therefore, exhibit predominantly surface DL centers [30]. In particular, DL of ZnO whiskers upon X-ray excitation peaked at 510 nm [30].

5. Conclusions

The technique of sputtering of a hot ceramic target was used to synthesize ZnO films of large thickness (more than 100 μm) at high speed. Post-growth plasma treatment of the films facilitated a significant increase in crystallinity and a decrease in the defective phase. The results obtained allow one to judge the prospects of using the fabricated films for detecting ionizing radiation. The transmission of such films is higher compared to other ZnO microstructures with a similar thickness. The plasma treatment of the samples resulted in the appearance of the fast NBEL band with a high intensity in the XRL spectrum (the origin of NBEL is mainly the near-surface regions of the films); though, DL with a microsecond decay time still contributes to XRL, which is an issue for further study. To improve the scintillation properties of the films, additional polishing is not required.

Analysis of data obtained by UV-vis, photoluminescence and X-ray luminescence spectroscopy elucidated luminescence mechanisms of the studied films at room temperature. The main contribution to the room temperature NBEL of the films is made by phonon replicas of free exciton radiation. In particular, under optical excitation, the NBEL band is formed predominantly by the X-LO radiation and less pronounced X-2LO radiation, which provides a long-wavelength shoulder to the main band. Under X-ray excitation, the NBEL band is formed mainly by X-2LO radiation, since the bulk of the X-LO emission is absorbed within the film's volume. The additional analysis of DL of the films showed that green luminescence band ($\lambda \sim 510$ nm) is due to surface emission centers, while green-yellow emission ($\lambda > 550$ nm) originates mainly from bulk parts of the films.

The data obtained can be used not only in studying the scintillation properties of ZnO structures, but also in general in the study of radiative processes in ZnO microobjects, including spontaneous and stimulated emission.

Author Contributions: Conceptualization, A.P.T. and A.E.M.; methodology, A.P.T., A.M.I., M.K.G., I.D.V., A.E.M., I.S.V., S.R.A., A.S.T. and A.V.B.; software, A.P.T., I.D.V., A.E.M. and I.S.V.; validation, A.P.T., I.D.V., A.E.M. and V.M.K.; formal analysis, A.P.T., I.D.V. and A.E.M.; investigation, A.P.T., A.M.I., M.K.G., I.D.V., A.E.M., I.S.V., S.R.A., A.S.T. and A.V.B.; resources, A.P.T., A.M.I., I.D.V., A.E.M. and V.M.K.; data curation, A.P.T., I.D.V. and A.E.M.; writing—original draft preparation, A.P.T., I.D.V. and A.E.M.; writing—review and editing, A.P.T.; visualization, A.P.T., I.D.V., A.E.M. and I.S.V.; supervision, A.P.T., A.E.M. and V.M.K.; project administration, A.P.T. and A.E.M.; funding acquisition, A.P.T. All authors have read and agreed to the published version of the manuscript.

Funding: The study was supported by the grant of the Russian Science Foundation (grant No. 23-29-00535, <https://rscf.ru/en/project/23-29-00535/> (accessed on 5 December 2023)).

Institutional Review Board Statement: Not applicable.

Informed Consent Statement: Not applicable.

Data Availability Statement: Data can be made available upon reasonable request.

Conflicts of Interest: The authors declare no conflict of interest.

References

1. Tsoulfanidis, N.; Landsberger, S. *Measurement and Detection of Radiation*; CRC Press: Boca Raton, FL, USA, 2021.
2. Seco, J.; Clasié, B.; Partridge, M. Review on the characteristics of radiation detectors for dosimetry and imaging. *Phys. Med. Biol.* **2014**, *59*, R303. [[CrossRef](#)] [[PubMed](#)]
3. Wei, H.; Huang, J. Halide lead perovskites for ionizing radiation detection. *Nat. Commun.* **2019**, *10*, 1066. [[CrossRef](#)] [[PubMed](#)]
4. Johns, P.M.; Nino, J.C. Room temperature semiconductor detectors for nuclear security. *J. Appl. Phys.* **2019**, *126*, 040902. [[CrossRef](#)]
5. Kharzheev, Y.N. Radiation Hardness of Scintillation Detectors Based on Organic Plastic Scintillators and Optical Fibers. *Phys. Part. Nuclei* **2019**, *50*, 42–76. [[CrossRef](#)]
6. Moses, W.W. Current trends in scintillator detectors and materials. *Nucl. Instrum. Methods Phys.* **2002**, *487*, 123–128. [[CrossRef](#)]

7. Afanasyev, V.I.; Kozlovskii, S.S.; Makar'in, D.V.; Mel'nik, A.D.; Mironov, M.I.; Nesenevich, V.G.; Petrov, M.P.; Petrov, S.Y.; Chernyshev, F.V. Background and radiation resistance tests of neutral particle analyzer detectors for ITER by using a fast neutron beam. *Plasma Phys. Rep.* **2010**, *36*, 407–412. [[CrossRef](#)]
8. Quarati, F.G.A.; Owens, A.; Dorenbos, P.; De Haas, J.T.M.; Benzoni, G.; Blasi, N.; Boiano, C.; Brambilla, S.; Camera, F.; Alba, R.; et al. High energy gamma-ray spectroscopy with LaBr₃ scintillation detectors. *Nucl. Instrum. Methods Phys.* **2011**, *629*, 157–169. [[CrossRef](#)]
9. Yanagida, T. Inorganic scintillating materials and scintillation detectors. *Proc. Jpn Acad. Ser. B Phys. Biol. Sci.* **2018**, *94*, 75–97. [[CrossRef](#)]
10. Cooper, J.C.; Koltick, D.S.; Mihalczko, J.T.; Neal, J.S. Evaluation of ZnO (Ga) coatings as alpha particle transducers within a neutron generator. *Nucl. Instrum. Methods Phys.* **2003**, *505*, 498–501. [[CrossRef](#)]
11. Jacobsson, T.J.; Viarbitskaya, S.; Mukhtar, E.; Edvinsson, T. A size dependent discontinuous decay rate for the exciton emission in ZnO quantum dots. *Phys. Chem. Chem. Phys.* **2014**, *16*, 13849–13857. [[CrossRef](#)]
12. Lecoq, P.; Gektin, A.; Korzhik, M. Addressing the Increased Demand for Fast Timing. In *Inorganic Scintillators for Detector Systems*, 2nd ed.; Lecoq, P., Gektin, A., Korzhik, M., Eds.; Springer: Berlin/Heidelberg, Germany, 2017; pp. 103–123. [[CrossRef](#)]
13. Kumar, V.; Luo, Z. A Review on X-ray Excited Emission Decay Dynamics in Inorganic Scintillator Materials. *Photonics* **2021**, *8*, 71. [[CrossRef](#)]
14. Sahani, R.M.; Dixit, A. A comprehensive review on zinc oxide bulk and nano-structured materials for ionizing radiation detection and measurement applications. *Mater. Sci. Semicond. Process* **2022**, *151*, 107040. [[CrossRef](#)]
15. Fonoberov, V.A.; Balandin, A.A. ZnO Quantum Dots: Physical Properties and Optoelectronic Applications. *J. Nanoelectron. Optoelectron.* **2006**, *1*, 19–38. [[CrossRef](#)]
16. Zhang, D.; Fan, P.; Cai, X.; Huang, J.; Ru, L.; Zheng, Z.; Liang, G.; Huang, Y. Properties of ZnO thin films deposited by DC reactive magnetron sputtering under different plasma power. *Appl. Phys. A* **2009**, *97*, 437–441. [[CrossRef](#)]
17. Capper, P.; Kasap, S.O.; Willoughby, A. *Zinc Oxide Materials for Electronic and Optoelectronic Device Applications*; John Wiley & Sons: Hoboken, NJ, USA, 2011.
18. Wang, F.H.; Chang, H.P.; Tseng, C.C.; Huang, C.C. Effects of H₂ plasma treatment on properties of ZnO: Al thin films prepared by RF magnetron sputtering. *Surf. Coat. Technol.* **2011**, *205*, 5269–5277. [[CrossRef](#)]
19. Djurišić, A.B.; Chen, X.; Leung, Y.H.; Ng, A.M.C. ZnO nanostructures: Growth, properties and applications. *J. Mat. Chem.* **2012**, *22*, 6526–6535. [[CrossRef](#)]
20. Pillai, S.C.; Kelly, J.M.; Ramesh, R.; McCormack, D.E. Advances in the synthesis of ZnO nanomaterials for varistor devices. *J. Mat. Chem. C* **2013**, *1*, 3268–3281. [[CrossRef](#)]
21. Leonardi, S.G. Two-Dimensional Zinc Oxide Nanostructures for Gas Sensor Applications. *Chemosensors* **2017**, *5*, 17. [[CrossRef](#)]
22. Mishra, Y.K.; Adelung, R. ZnO tetrapod materials for functional applications. *Mat. Today* **2018**, *21*, 631–651. [[CrossRef](#)]
23. Borysiewicz, M.A. ZnO as a Functional Material, a Review. *Crystals* **2019**, *9*, 505. [[CrossRef](#)]
24. Faramawy, A.; Elsayed, H.; Scian, C.; Mattei, G. Structural, Optical, Magnetic and Electrical Properties of Sputtered ZnO and ZnO:Fe Thin Films: The Role of Deposition Power. *Ceramics* **2022**, *5*, 1128–1153. [[CrossRef](#)]
25. Chang, Y.-C.; Lin, Y.-R.; Chen, S.-W.; Chou, C.-M. Density-Controlled Growth of ZnO Nanowalls for High-Performance Photocatalysts. *Materials* **2022**, *15*, 9008. [[CrossRef](#)] [[PubMed](#)]
26. Sharma, D.K.; Shukla, S.; Sharma, K.K.; Kumar, V. A review on ZnO: Fundamental properties and applications. *Mater. Today Proc.* **2022**, *49*, 3028–3035. [[CrossRef](#)]
27. Ji, J.; Colosimo, J.J.; Anwand, A.M.; Boatner, W.; Wagner, L.A.; Stepanov, A.; Trinh, T.T.; Liedke, M.O.; Krause-Rehberg, R.; Cowan, T.E.; et al. ZnO Luminescence and scintillation studied via photoexcitation, X-ray excitation and gamma-induced positron spectroscopy. *Sci. Rep.* **2016**, *6*, 31238. [[CrossRef](#)] [[PubMed](#)]
28. Crapanzano, R.; Villa, I.; Mostoni, S.; D'Arienzo, M.; Di Credico, B.; Fasoli, M.; Scotti, R.; Vedda, A. Morphology Related Defectiveness in ZnO Luminescence: From Bulk to Nano-Size. *Nanomaterials* **2020**, *10*, 1983. [[CrossRef](#)]
29. Li, Q.; Liu, X.; Gu, M.; Hu, Y.; Li, F.; Liu, S.; Wu, Q.; Sun, Z.; Zhang, J.; Huang, S.; et al. Development of ZnO-based nanorod arrays as scintillator layer for ultrafast and high-spatial-resolution X-ray imaging system. *Opt. Exp.* **2018**, *26*, 31290–31298. [[CrossRef](#)]
30. Venetsev, I.D.; Tarasov, A.P.; Muslimov, A.E.; Gorokhova, E.I.; Zadorozhnaya, L.A.; Rodnyi, P.A.; Kanevsky, V.M. Ultraviolet Luminescence of ZnO Whiskers, Nanowalls, Multipods, and Ceramics as Potential Materials for Fast Scintillators. *Materials* **2021**, *14*, 2001. [[CrossRef](#)] [[PubMed](#)]
31. Tarasov, A.P.; Venetsev, I.D.; Muslimov, A.E.; Zadorozhnaya, L.A.; Rodnyi, P.A.; Kanevsky, V.M. Luminescent properties of a ZnO whisker array as a scintillation detector material. *Quantum Electron.* **2021**, *51*, 366–370. [[CrossRef](#)]
32. Simpson, P.J.; Tjossem, R.; Hunt, A.W.; Lynn, K.G.; Munné, V. Superfast timing performance from ZnO scintillators. *Nucl. Instrum. Methods Phys.* **2003**, *505*, 82–84. [[CrossRef](#)]
33. Demidenko, V.A.; Gorokhova, E.I.; Khodyuk, I.V.; Ol'ga, A.K.; Mikhrin, S.B.; Rodnyi, P.A. Scintillation properties of ceramics based on zinc oxide. *Rad. Meas.* **2007**, *42*, 549–552. [[CrossRef](#)]
34. Bourret-Courchesne, E.D.; Derenzo, S.E.; Weber, M.J. Development of ZnO: Ga as an ultra-fast scintillator. *Nucl. Instrum. Methods Phys.* **2009**, *601*, 358–363. [[CrossRef](#)]

35. Neal, J.S.; Giles, N.C.; Yang, X.; Wall, R.A.; Ucer, K.B.; Williams, R.T.; Wisniewski, D.J.; Boatner, L.A.; Rengarajan, V.; Nause, J.; et al. Evaluation of melt-grown, ZnO single crystals for use as alpha-particle detectors. *IEEE Trans. Nucl. Sci.* **2008**, *55*, 1397–1403. [[CrossRef](#)]
36. Look, D.C. Recent advances in ZnO materials and devices. *Mat. Sci. Eng. B* **2001**, *80*, 383–387. [[CrossRef](#)]
37. Avrutin, V.; Cantwell, G.; Zhang, J.; Song, J.J.; Silversmith, D.J.; Morkoç, H. Bulk ZnO: Current status, challenges, and prospects. *Proc. IEEE* **2010**, *98*, 1339–1350. [[CrossRef](#)]
38. Fan, L.; Zhong, C.; Wang, X.J.; Cao, L.; Wang, J.; Peng, L.; Zhan, Z.; Xiong, Z.; Wu, W. Heterogeneous Growth of ZnO Crystal on GaN/Al₂O₃ Substrate. *Wuhan Univ. Technol. Mater. Sci. Ed.* **2022**, *37*, 576–579. [[CrossRef](#)]
39. Nesenevich, V.G.; Afanasyev, V.I.; Kozlovskii, S.S.; Makar'in, D.V.; Mel'nik, A.D.; Mironov, M.I.; Petrov, M.P.; Petrov, S.Y.; Chernyshev, F.V. A comparative analysis of the sensitivity of CsI (Tl), ZnO (Ga), and YAG (Ce) scintillators to the plasma background radiation under operating conditions of the ITER tokamak reactor. *Instrum. Exp. Technol.* **2012**, *55*, 255–258. [[CrossRef](#)]
40. Wen, X.; Zhang, Q.; Shao, Z. Magnetron Sputtering for ZnO:Ga Scintillation Film Production and Its Application Research Status in Nuclear Detection. *Crystals* **2019**, *9*, 263. [[CrossRef](#)]
41. Muslimov, A.E.; Kanevsky, V.M.; Venevtsev, I.D.; Ismailov, A.M. Optical Properties of Thick Zinc Oxide Films Doped with Gallium and Gold. *Cryst. Rep.* **2020**, *65*, 766–771. [[CrossRef](#)]
42. Venevtsev, I.D.; Rodnyi, P.A.; Muslimov, A.E.; Kanevskii, V.M.; Babaev, V.A.; Ismailov, A.M. X-Ray Luminescence of Zinc Oxide Thick Films. *Opt. Spectrosc.* **2019**, *127*, 1075–1079. [[CrossRef](#)]
43. Ismailov, A.M.; Nikitenko, V.A.; Rabadanov, M.R.; Emiraslanova, L.L.; Aliev, I.S.; Rabadanov, M.K. Sputtering of a hot ceramic target: Experiments with ZnO. *Vacuum* **2019**, *168*, 108854. [[CrossRef](#)]
44. Gadzhiev, M.K.; Kulikov, Y.M.; Son, E.E.; Tyuftyaev, A.S.; Sargsyan, M.A.; Yusupov, D.I. Efficient Generator of Low-temperature Argon Plasma with an Expanding Channel of the Output. *High Temp.* **2020**, *58*, 12–20. [[CrossRef](#)]
45. Biberman, L.M.; Vorobiev, V.S.; Yakubov, I.T. *Kinetics of Nonequilibrium Low-Temperature Plasma*; Nauka: Moscow, Russia, 1982. (In Russian)
46. Muslimov, A.E.; Asadchikov, V.E.; Butashin, A.V.; Vlasov, V.P.; Deryabin, A.N.; Roshchin, B.S.; Kanevsky, V.M. Supersmooth and modified surface of sapphire crystals: Formation, characterization, and applications in nanotechnologies. *Cryst. Rep.* **2016**, *61*, 730–743. [[CrossRef](#)]
47. Rodnyi, P.A.; Mikhlin, S.B.; Mishin, A.N.; Sidorenko, A.V. Small-size pulsed X-ray source for measurements of scintillator decay time constants. *IEEE Trans. Nucl. Sci.* **2001**, *48*, 2340–2343. [[CrossRef](#)]
48. Pashley, D.W. Recent Developments in the Study of Epitaxy. *Resent Prog. Surf. Sci.* **1970**, *3*, 23–69. [[CrossRef](#)]
49. Kozhevnikov, I.V.; Buzmakov, A.V.; Siewert, F.; Tiedtke, K.; Störmer, M.; Samoylova, L.; Sinn, H. Growth of nano-dots on the grazing-incidence mirror surface under FEL irradiation. *J. Synchrotron Rad.* **2016**, *23*, 78–90. [[CrossRef](#)] [[PubMed](#)]
50. Xie, J.Q.; Dong, J.W.; Osinsky, A.; Chow, P.P.; Heo, Y.W.; Norton, D.P.; Pearton, S.J.; Dong, X.Y.; Adelman, C.; Palmström, C.J. Growth of a-plane ZnO Thin Films on r-plane Sapphire by Plasma-assisted MBE. *MRS Online Proc. Libr.* **2005**, *891*, 1001. [[CrossRef](#)]
51. Monshi, A.; Foroughi, M.R.; Monshi, M.R. Modified Scherrer equation to estimate more accurately nano-crystallite size using XRD. *World J. Nano Sci. Eng.* **2012**, *2*, 154–160. [[CrossRef](#)]
52. Muniz, F.T.L.; Miranda, M.R.; Morilla dos Santos, C.; Sasaki, J.M. The Scherrer equation and the dynamical theory of X-ray diffraction. *Acta Crystallogr. A* **2016**, *72*, 385–390. [[CrossRef](#)]
53. Rabiei, M.; Palevicius, A.; Monshi, A.; Nasiri, S.; Vilkauskas, A.; Janusas, G. Comparing Methods for Calculating Nano Crystal Size of Natural Hydroxyapatite Using X-Ray Diffraction. *Nanomaterials* **2020**, *10*, 1627. [[CrossRef](#)]
54. Ozgur, U.; Alivov, Y.I.; Liu, C.; Teke, A.; Reshchikov, M.A.; Dogan, S.; Avrutin, V.; Cho, S.J.; Morkoc, H. A comprehensive review of ZnO materials and devices. *J. Appl. Phys.* **2005**, *98*, 41301. [[CrossRef](#)]
55. Galdámez-Martinez, A.; Santana, G.; Güell, F.; Martínez-Alanis, P.R.; Dutt, A. Photoluminescence of ZnO Nanowires: A Review. *Nanomaterials* **2020**, *10*, 857. [[CrossRef](#)] [[PubMed](#)]
56. Lv, J.; Li, C.; Chai, Z. Defect luminescence and its mediated physical properties in ZnO. *J. Lumin.* **2019**, *208*, 225–237. [[CrossRef](#)]
57. Wang, L.; Giles, N.C. Temperature dependence of the free-exciton transition energy in zinc oxide by photoluminescence excitation spectroscopy. *J. Appl. Phys.* **2003**, *94*, 973–978. [[CrossRef](#)]
58. Klingshirn, C.; Fallert, J.; Zhou, H.; Sartor, J.; Thiele, C.; Maier-Flaig, F.; Schneider, D.; Kalt, H. 65 years of ZnO research—old and very recent results. *Phys. Status Solidi* **2010**, *247*, 1424–1447. [[CrossRef](#)]
59. Tarasov, A.P.; Muslimov, A.E.; Kanevsky, V.M. Excitonic Mechanisms of Stimulated Emission in Low-Threshold ZnO Microrod Lasers with Whispering Gallery Modes. *Materials* **2022**, *15*, 8723. [[CrossRef](#)]
60. Son, E.E.; Gadzhiev, M.K.; Kulikov, Y.M. Plasma Disposal in Problems of Ecology (Review). *High Temp.* **2020**, *58*, 495–519. [[CrossRef](#)]
61. Klingshirn, C.F. *Semiconductor Optics*, 4th ed.; Springer: Berlin/Heidelberg, Germany, 2012.
62. Versteegh, M.A.; Kuis, T.; Stoof, H.T.C.; Dijkhuis, J.I. Ultrafast screening and carrier dynamics in ZnO: Theory and experiment. *Phys. Rev. B* **2011**, *84*, 035207. [[CrossRef](#)]

Disclaimer/Publisher's Note: The statements, opinions and data contained in all publications are solely those of the individual author(s) and contributor(s) and not of MDPI and/or the editor(s). MDPI and/or the editor(s) disclaim responsibility for any injury to people or property resulting from any ideas, methods, instructions or products referred to in the content.